Eur. Phys. J. D (2025)79:93
https://doi.org/10.1140/epjd/s10053-025-01036-4

THE EUROPEAN PHYSICAL JOURNAL D

Regular Article – Ultraintense and Ultrashort Laser Fields

Elimination of spurious oscillations on photoemission spectra

Martín Barlari[1,2,a], Diego G. Arbó[1,2,3], María Silvia Gravielle[1], and Darío M. Mitnik[1]

[1] Instituto de Astronomía y Física del Espacio - IAFE (CONICET-UBA), 1428 Buenos Aires, Argentina
[2] Facultad de Ciencias Exactas y Naturales, Departamento de Física, Universidad de Buenos Aires, 1428 Buenos Aires, Argentina
[3] Universidad de Buenos Aires, Ciclo Básico Común, Buenos Aires, Argentina

Received 27 April 2025 / Accepted 29 June 2025

Abstract. We present a method for accurately computing transition probabilities in one-dimensional photoionization problems. Our approach involves solving the time-dependent Schrödinger equation and projecting its solution onto scattering states that satisfy the correct incoming or outgoing boundary conditions. Conventionally, the photoelectron emission spectrum is obtained by projecting the time-evolved wave function onto the stationary continuum eigenstates of the unperturbed, time-independent Hamiltonian. However, when the spatial potential is symmetric, both the initial bound state and the final continuum states exhibit well-defined parity. The propagated wave function retains structural features of the initial bound state, including its parity. As a result, changes in the parity of the continuum states can introduce substantial variations in the projections, leading to spurious oscillations in the computed electron emission spectrum. Our method circumvents this issue by employing scattering states without defined parity. Furthermore, it enables the calculation of directional emission, making it possible to study emission asymmetries. To illustrate the capabilities of our scattering projection method, we analyze the partial differential photoionization probabilities of Al(111) metallic surfaces under short laser pulses at grazing incidence.

1 Introduction

Many ionization experiments aimed at obtaining energy spectra and cross sections are performed under quasi-stationary conditions. Consequently, quantum mechanics and scattering theory have traditionally focused on solutions of the time-independent Schrödinger equation, primarily because stationary scattering states form a basis that facilitates the analysis of time-dependent collisions. However, recent breakthroughs in laser technology—particularly the advent of attosecond pulses, a key achievement recognized by the 2023 Nobel Prize in Physics [1]—have sparked growing interest in ultrashort laser pulses as ionizing sources. As a result, theoretical approaches must adapt to these developments by placing greater emphasis on the temporal description of physical processes.

The calculation of photoionization spectra has been an active area of research for several decades, encompassing a wide variety of targets, including atoms [2–5], molecules [6–8], and solids [9–11]. In many cases—such as electron emission from solid surfaces—the underlying physics can be effectively described using one-dimensional models [12,13]. For instance, photoemission from the valence band has been studied for metallic surfaces like Al(111), Al(100), Be(0001), and Mg(0001) [12,13].

Following previous studies [12–17], photoelectron spectra are commonly obtained by numerically solving the time-dependent Schrödinger equation (TDSE) and projecting the final wave function onto the stationary continuum eigenstates of the unperturbed time-independent Hamiltonian. However, this approach often yields large unphysical oscillations in the energy spectrum [12,14]. To mitigate these artifacts, convolution techniques such as the widely used window-operator method (WOM) [18,19] are typically employed. Nevertheless, we have found that these methods can inadvertently suppress physically meaningful structures in the spectrum.

In this work, we restrict our study to one-dimensional ionization processes and perform a detailed analysis of electron emission from symmetric potentials. To overcome the aforementioned spurious oscillations, we introduce a computational method that projects the wave function—evaluated at the end of the laser pulse—onto scattering states with the appropriate incoming or outgoing boundary conditions. Our scattering projection method (SPM) not only eliminates the unphysical oscillations more effectively than the WOM but also preserves fine structures of physical relevance, such as

[a] e-mail: mbarlari@iafe.uba.ar (corresponding author)

Published online: 03 August 2025

Ramsauer–Townsend-type oscillations, which are otherwise suppressed by the WOM.

We investigate the ionization of a one-electron system subjected to an external electric field, modeled as either a traveling wave (short laser pulse) or a standing wave (half-cycle pulse). We begin with a simple square-well potential supporting a single bound state, then proceed to the jellium model [14] as a first approximation of a metallic surface, and finally apply a more sophisticated band-structure-based (BSB) potential for Al(111), which incorporates surface roughness due to atomic layering as well as surface plasmon effects [13,20].

This article is organized as follows. In Sect. 2, we describe the numerical methods used to solve the TDSE for electron ionization in a one-dimensional potential, and we detail two approaches to extract the energy spectrum: (i) projection onto standard stationary continuum eigenstates of the time-independent Schrödinger equation (TISE), and (ii) the proposed SPM using scattering states. A step-by-step numerical procedure is provided in the Appendix A. In Sect. 3, we present and compare results for simple potentials obtained via both projection techniques and the WOM. In Sect. 4, we apply the methods to the photoionization of metallic surfaces. Finally, Sect. 5 summarizes our findings and outlines future directions for the systematic study of metal photoionization under ultrashort laser pulses. Unless otherwise stated, atomic units are used throughout.

2 Theory

2.1 Resolution of the time-dependent Schrödinger equation

We consider the ionization of a one-dimensional system consisting of a single electron bound in a short-range potential $V(z)$ and subjected to an external time-dependent electric field. Within the dipole approximation, the time-dependent Schrödinger equation (TDSE) takes the form

$$i\frac{\partial}{\partial t}|\psi(t)\rangle = [H_0 + H_{\rm int}(t)]\,|\psi(t)\rangle, \tag{1}$$

where the unperturbed Hamiltonian is $H_0 = p^2/2 + V(z)$, with the first term representing the kinetic energy of the electron, and the second term describing its interaction with an attractive potential that models, for example, an atom, molecule, or solid-state system. The momentum p corresponds to the conjugate operator of the position operator z. In general, as the electron escapes from the region where the potential is considerable toward the detector, where $V(z \to \infty) = 0$, p varies from an initial value to the asymptotic value k. Whereas the momentum p (and the kinetic energy) varies with time, the asymptotic momentum k is a constant of motion and therefore a good quantum number.

The term $H_{\rm int}(t)$ accounts for the interaction with the external field. In the length gauge, this interaction is given by $H_{\rm int}(t) = zF(t)$, where $F(t)$ is the time-dependent electric field. Under the influence of this field, an electron initially in a bound state $|\phi_i\rangle$ can be excited to another bound state $|\phi_n\rangle$ with energy E_n, or ionized into the continuum, ending in a state $|\phi_k\rangle$ characterized by asymptotic momentum k and energy $E = k^2/2$.

To numerically solve Eq. (1), we use the staggered leap-frog method [21,22]. This is a robust time propagation technique commonly applied in the simulation of atomic and molecular few-body dynamics [23]. The method provides an efficient and stable approach to evolving the wave function under the influence of strong and time-dependent external fields.

2.2 Projection onto stationary waves

Once the TDSE [Eq. (1)] has been solved, the time-propagated wave function $\psi(z,t) = \langle z|\psi(t)\rangle$ is available. After the conclusion of the electric pulse of duration τ, the electron is subject only to the influence of the time-independent potential $V(z)$. Therefore, the kinetic energy is conserved and the asymptotic momentum k is a good quantum number. In this paper, we consider only short-range symmetric potentials, i.e., $V(z) = V(-z)$. Hence, both the bound $\phi_j(z)$ and continuum $\phi_k(z)$ eigenstates of the time-independent Hamiltonian H_0 have definite parity, which means that they will be either even $[\phi_i^{(e)}(z) = \phi_i^{(e)}(-z)]$ or odd $[\phi_i^{(o)}(z) = -\phi_i^{(o)}(-z)]$. The wave function $\psi(z,\tau)$ at the end of the interaction with the external force can be written as a linear combination of stationary eigenstates

$$|\psi(\tau)\rangle = \sum_j^{N_b} a_j|\phi_j\rangle + \int_{-\infty}^{\infty} dk\, a_k|\phi_k\rangle\,, \tag{2}$$

where N_b is the number of bound states of $V(z)$, and the transition amplitudes for bound and continuum states are

$$a_i = \langle\phi_i\,|\,\psi(\tau)\rangle\,. \tag{3}$$

The differential probability of electron emission can be expressed as a function of the electron momentum k or the kinetic energy E as

$$\frac{dP}{dE} = k\frac{dP}{dk} = \sqrt{2E}\,|a_k|^2\,. \tag{4}$$

If the continuum states are degenerate, the photoelectron emission probability is

$$\frac{dP}{dE} = k\frac{dP}{dk} = \sqrt{2E}\left(|a_k^{(e)}|^2 + |a_k^{(o)}|^2\right)\,, \tag{5}$$

where the amplitudes $a_k^{(q)}$ correspond to the projections over the degenerate eigenfunctions $H_0|\phi_k^{(q)}\rangle = E_k|\phi_k^{(q)}\rangle$, for $q = e, o$.

If the TISE is solved numerically in a spatial grid with a large but finite number of grid points N within a bounded (1D) spatial range (referred to as "the box"), the Hamiltonian spectrum becomes L^2 finite and discrete even in the region where $(E > 0)$. The differential photoelectron emission probability can be recovered as

$$\frac{dP}{dE} \simeq \frac{|a_n|^2}{\Delta E_n} \qquad \text{if} \quad E_n > 0\,, \tag{6}$$

where we have approximated the differential dE for a discrete energy bin of size ΔE_n, which takes into account the density of states. In this context, the index of the eigenfunction n determines the parity of the eigenfunction. From Eq. (6), we can express the total ionization probability P_{ion} as follows:

$$P_{\text{ion}} = \int_0^\infty dE \left(\frac{dP}{dE}\right) \simeq \sum_{n=N_b+1}^{N} |a_n|^2, \tag{7}$$

where the continuous integral over the energy was approximated for a discrete sum involving the $N - N_b$ eigenstates with $E_n > 0$.

2.3 Scattering projection method

We can alternatively project the final state $|\psi(t)\rangle$ onto a different basis of continuous states, which have non-definite parity. In this work, we propose the scattering projection method (SPM), in which the projection basis consists of scattering waves that meet the appropriate asymptotic conditions. Given that the one-dimensional potential well is a short-range potential, the scattering waves with incoming (+) boundary conditions—related to plane-wave incidence from the right (r) and from the left (l)—asymptotically behave as follows:

$$\Psi_k^{(r,+)}(z) = \begin{cases} T_r^{(+)}(k)e^{-ikz} & \text{if } z \to -\infty \\ e^{-ikz} + R_r^{(+)}(k)e^{ikz} & \text{if } z \to +\infty \end{cases} \tag{8a}$$

$$\Psi_k^{(l,+)}(z) = \begin{cases} e^{ikz} + R_l^{(+)}(k)e^{-ikz} & \text{if } z \to -\infty \\ T_l^{(+)}(k)e^{ikz} & \text{if } z \to +\infty \end{cases} \tag{8b}$$

Similarly, the scattering waves with outgoing (-) boundary conditions, associated with the plane-wave emissions to the right (r) and the left (l), behave asymptotically as:

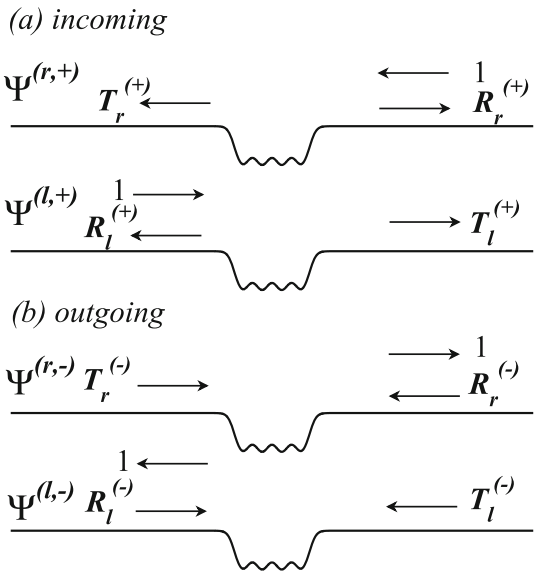

Fig. 1 Scheme of scattering waves in a one-dimensional well. **a** Incoming scattering waves from the right $\Psi_k^{(r,-)}$ and from the left $\Psi_k^{(l,-)}$ and **b** outgoing scattering waves to the right $\Psi_k^{(r,+)}$ and to the left $\Psi_k^{(l,+)}$

$$\Psi_k^{(r,-)}(z) = \begin{cases} T_r^{(-)}(k)e^{ikz} & \text{if } z \to -\infty \\ e^{ikz} + R_r^{(-)}(k)e^{-ikz} & \text{if } z \to +\infty \end{cases} \tag{9a}$$

$$\Psi_k^{(l,-)}(z) = \begin{cases} e^{-ikz} + R_l^{(-)}(k)e^{ikz} & \text{if } z \to -\infty \\ T_l^{(-)}(k)e^{-ikz} & \text{if } z \to +\infty \end{cases}. \tag{9b}$$

In Eqs. (8) and (9) $R_{r(l)}^{(\pm)}(k)$ and $T_{r(l)}^{(\pm)}(k)$ are the respective right (left) reflection and transmission coefficients with the corresponding asymptotic boundary conditions $(\pm)$. As it is well known, both the incoming basis $\{\Psi^{(r,+)}, \Psi^{(l,+)}\}$ and the outgoing basis $\{\Psi^{(r,-)}, \Psi^{(l,-)}\}$ can be used to describe the continuous states of the scattering problem (1).

In the specific case of a square-well potential, the scattering wave functions can be derived analytically [24]. For other potentials where the analytical scattering wave functions are either challenging to obtain or do not exist, we introduce a plane-wave basis using a procedure based on Ref. [25]. In Appendix A, we demonstrate how to numerically calculate the transmission and reflection coefficients for a given short-range potential. Once the scattering states are established, the photoemission probabilities can be retrieved within the SPM framework by projecting the time-propagated wave function onto the incoming (+) or outgoing (-) basis, similar to the process outlined in Eq. (5). That

is [26],

$$\left(\frac{dP}{dE}\right)^{(+)}_{\rm SPM} = \sqrt{2E}\left(|\langle\Psi_k^{(l,+)}|\psi(\tau)\rangle|^2 + |\langle\Psi_k^{(r,+)}|\psi(\tau)\rangle|^2\right), \quad (10a)$$

$$\left(\frac{dP}{dE}\right)^{(-)}_{\rm SPM} = \sqrt{2E}\left(|\langle\Psi_k^{(l,-)}|\psi(\tau)\rangle|^2 + |\langle\Psi_k^{(r,-)}|\psi(\tau)\rangle|^2\right), \quad (10b)$$

respectively, and both expressions are equivalent.

2.4 Window-operator method

We provide a brief overview of the widely used window-operator method (WOM), developed by Schafer [18,19], for extracting energy-resolved probabilities from a wave function calculated on a numerical grid. This method approximates the differential emission probability by evaluating the expectation value of the window (or tapering) operator on the time-evolved wave function $|\psi(\tau)\rangle$

$$P(E) \approx \langle\psi(\tau)|\hat{W}|\psi(\tau)\rangle = \langle\psi(\tau)|\frac{\gamma^{2^n}}{(H_0-E)^{2^n}+\gamma^{2^n}}|\psi(\tau)\rangle\,. \quad (11)$$

Expanding the final numerical state into stationary wave functions, Eq. (11) becomes

$$P(E) = \int_{-\infty}^{\infty} dk \frac{k\ \gamma^{2^n}}{\left(\frac{k^2}{2}-E\right)^{2^n}+\gamma^{2^n}}\left|\langle\phi_k|\ \psi(\tau)\rangle\right|^2, \quad (12)$$

which can be interpreted as the convolution of the amplitude $|\langle\phi_k|\psi(\tau)\rangle|^2$ with the window-operator function. In Eq. (12), we deal with eigenstates $|\phi_k\rangle$ in the continuum of energy; however, both bound and continuum states can be treated using the WOM. The two parameters of the window function, γ and n, must be adjusted to obtain resolved and accurate energy spectra. For example, $n = 1$ corresponds to a Lorentzian window, and as n increases, the window approaches a rectangular shape, thus reducing the overlap between adjacent energy bins.

The results obtained with the WOM are proportional to the ionization probability, up to a constant factor related to the energy width 2γ of the WOM. Consequently, $P(E)$ exhibits a vertical shift that depends on γ [19,27]. In our case, we do not compare individual final probabilities for each eigenstate of the numerical box but the energy spectrum, i.e., the energy distribution in the continuum [Eq. (6)]. Due to the quasi-rectangular shape of $P(E)$ for $n \geq 2$, the distribution becomes (Eq. (8) of [19]).

$$\left(\frac{dP}{dE}\right)_{\rm W} = \frac{P(E)}{2\gamma} \quad (13)$$

As long as γ is small compared with the characteristic variations of $P(E)$ yet still larger than the energy-grid spacing ΔE_i, the shape of the energy distribution remains essentially unchanged; only an overall scaling proportional to γ is introduced. In the limiting case $\gamma \sim \Delta E_i$ and $E = E_i$, the WOM leaves the energy distribution obtained from the stationary eigenstates of the numerical box unchanged.

3 Results for simple models

We evaluate different projection methods by calculating the electron emission spectra resulting from photoionization of a target subjected to an external linearly polarized laser, whose time-dependent electric field is given by

$$F(t) = F_0 \sin^2\left(\frac{\pi t}{\tau}\right)\cos(\omega t) \qquad t \in (0,\tau)\,, \quad (14)$$

where F_0 indicates the maximal strength of the electric pulse of main frequency ω and total duration τ.

In order to understand the origin of the spurious oscillations commonly observed in the theoretical photoionization spectra, we start considering a laser interacting with an electron confined within a square potential well. This potential has a width of $a = 3$ a.u. and depth $V_0 = 0.5$. It features a single bound state ϕ_1 with an energy of $E_1 = -0.314$ a.u.. The laser pulse has a frequency of $\omega = 0.8$ a.u., peak field strength of $F_0 = 0.5$, and a duration of six cycles, i.e., $\tau = 6 \times 2\pi/\omega = 47.12$ a.u.. We solve the TDSE as given by Eq. (1) in the length gauge, where $H_{\rm int}(t) = zF(t)$. The spatial grid for our calculations consists of $N = 5000$ points evenly distributed over $z = (-L/2, L/2)$ with $L = 200$ a.u.. The stationary eigenfunctions are obtained by diagonalizing the H_0 Hamiltonian using the LAPACK package [28]. For the TDSE solution, we utilize the staggered leap-frog method [21,22], propagating the wave functions over 60000 time steps with $\Delta t = 8.3 \times 10^{-4}$ a.u. until a time slightly greater than the pulse duration. Throughout the propagation, we continuously monitor the proper normalization of the wave function to ensure unitarity.

3.1 Differential emission probabilities

The photoionization emission probability is usually calculated by projecting the solution of the TDSE at the end of the laser pulse onto the continuum stationary eigenvectors. We computed the probabilities using Eq. (6) and present the outcome in Fig. 2. The expected photoelectron emission spectra consist of

broad peaks resulting from the multiphoton absorption process from the initial bound state. These peaks correspond to above-threshold ionization (ATI) energy levels ($n = 1, 2, \ldots$) and are separated by a photon energy of $\omega = 0.8$ a.u., in accordance with the energy conservation relation given by

$$E_n = n\omega - I_p - U_p\,. \tag{15}$$

In this context, the ionization potential is the binding energy of the initial state, $I_p = |E_1| = 0.314$ a.u., while the ponderomotive potential $U_p = [F_0/(2\omega)]^2 \simeq 0.1$ represents the energy of an oscillating electron influenced solely by the laser field [2].

However, the resulting spectra exhibit a strong oscillating pattern superimposed on the expected curves. These rapid oscillations cover an amplitude of about two orders of magnitude, and the spacing between their peaks increases as the emitted electron energy increases. It becomes evident [26] that the strong oscillatory structures within the peaks are a spurious artifact of the finite basis set used in the calculations. The explanation for these unexpected oscillations is straightforward. Projecting onto continuum functions results in two types of transition amplitude: one type, where both the continuum component of $\psi(\tau)$ and the projected ϕ_k waves have mostly the same parity, retains nearly the entire probability. The other type, in which the projected wave functions have opposite parities, exhibits significantly lower probabilities. When the physical problem is confined to a numerical grid, it is possible to move arbitrarily the walls of the box, changing thus the stationary eigenfunctions. It is possible then to design two potentials in which the same eigenvalue appears in both cases, but the corresponding eigenvectors have different parities. Therefore, the highly oscillating structures interfering with the ATI photoemission spectra are indeed spurious and should be disregarded.

To reduce the high oscillations in the total energy spectrum, we initially employed the WOM method using Eq. (12) with $\gamma = 0.045$ and examined three different values of $n = 1, 2$, and 3, as illustrated in Fig. 2a. On the one hand, we find that the high-frequency fluctuations vanish within the WOM approach. Additionally, while the broad multiphoton peaks are somewhat smeared for $n = 1$, they become well-defined with increasing values of n, with $n = 3$ being sufficient for an acceptable resolution. In Fig. 2b, we set $n = 3$ and analyze the calculated spectrum for three distinct γ values: 0.07, 0.045, and 0.02 a.u. The near-threshold structure, with peaks at approximately $E \simeq 0$ and 0.2 a.u., necessitates a narrow window with $\gamma = 0.02$ a.u. However, at high energy, near the third multiphoton peak at $E \sim 2$ a.u., the spurious oscillations are not completely smoothed, even with this γ value. Thus, a compromise must be struck to find a suitable γ value that addresses the near-threshold structures while mitigating the spurious oscillations at higher energies, which can sometimes prove challenging.

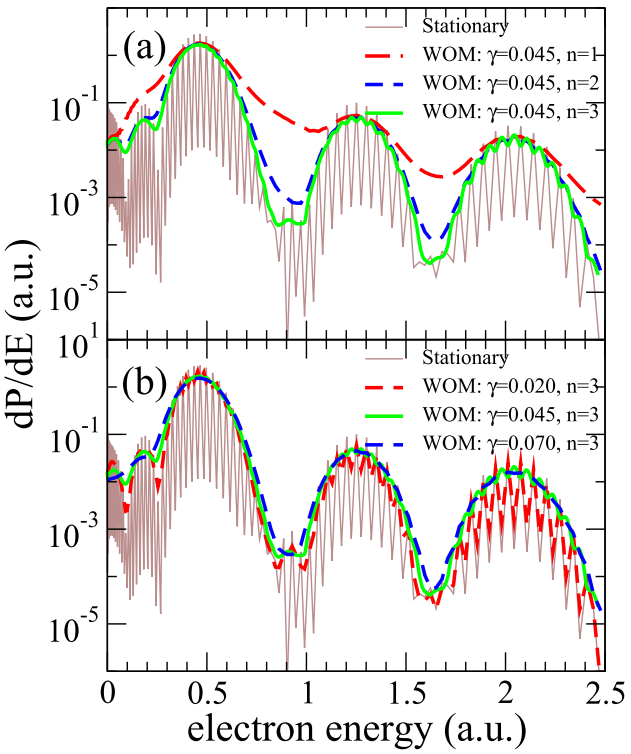

Fig. 2 Ionization differential emission probabilities for an electron confined in a square well with $a = 3$ a.u. and $V_0 = 0.5$ a.u. subject to a laser pulse given by Eq. (14) with $\omega = 0.8$ a.u., $F_0 = 0.5$, and $\tau = 47.12$ a.u.. **a** Projections onto stationary eigenstates (highly oscillating thin brown solid line) and WOM results with $\gamma = 0.045$, for $n = 1$ (dash red), 2 (dash blue), and 3 (dash green). **b** Projections onto stationary eigenfunctions (thin brown solid line), and WOM results with $n = 3$ $\gamma = 0.02$ (short dash red), 0.045 (solid green), and 0.07 (dash blue) lines

We then compare the outcome of the WOM with the electron emission spectrum obtained using our SPM. This was calculated by projecting the wave function at the end of the pulse, $\psi(z, \tau)$, onto the scattering waves $\Psi_k^{(l,\pm)}(z)$ and $\Psi_k^{(r,\pm)}(z)$, as described in Eqs. (10a) and (10b). The photoelectron emission differential probability $(dP/dE)_{\rm SPM}^{(\pm)}$ calculated from those equations is shown in Fig. 3. As expected, both results are consistent with one another. Notably, utilizing the SPM yields a significantly better resolution of the physical structures across the entire energy spectrum compared to the WOM approach. For instance, the near-threshold structures and the secondary peaks between the multiphoton peaks at approximately $E \simeq 0.9$ a.u. and 1.65 a.u. are much more clearly resolved. In addition, the small oscillations still visible in the second and third multiphoton peaks, reminiscent of the spurious high-frequency peaks within the WOM, are entirely washed out within the SPM. We have also investigated on the applicability of the SPM and WOM on soft-core hydrogenic potentials (see Appendix B).

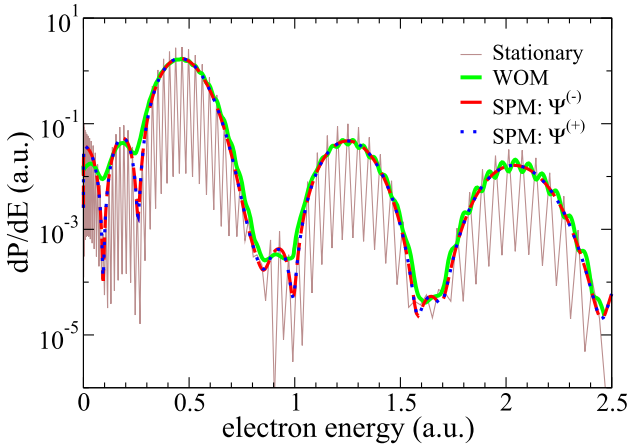

Fig. 3 Photoelectron emission probabilities from ϕ_1. Thin brown solid line: projection onto L^2 stationary eigenstates. Dash blue line: $(dP/dE)^{(+)}_{\rm SPM}$, i.e., projection onto incoming $\Psi^{(+)}$ scattering wave. Solid red line: $(dP/dE)^{(-)}_{\rm SPM}$. Green line: window filtered spectra with $\gamma = 0.045$ and $n = 3$

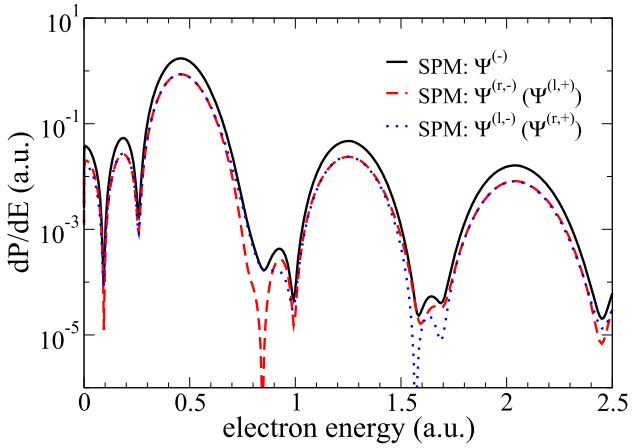

Fig. 4 Projection of the photoelectron spectrum from the only bound state of the same square well and subject to the same laser pulse as in Figs. 2 and 3 onto the scattering wave outgoing from the right $\Psi^{(r,-)}$ or equivalently incoming to the left $\Psi^{(l,+)}$ (see text) in dashed red line, outgoing from the left $\Psi^{(l,-)}$ or equivalently incoming to the right $\Psi^{(r,+)}$ in blue dotted line, and the sum of the two, i.e., projecting onto $\Psi^{(-)}$ or equivalently onto $\Psi^{(+)}$ in black solid line

3.2 Directional emission

So far, we have analyzed the total emission spectrum without considering the emission direction. In one dimension, photoelectrons can be emitted either to the right (forward, along the polarization direction $\hat{\mathbf{z}}$) or to the left (backward). To compute directional emission, we project the final wave function onto the outgoing scattering states $\Psi_k^{(r,-)}(z)$ for emission to the right and $\Psi_k^{(l,-)}(z)$ for emission to the left:

$$\left(\frac{dP}{dE}\right)_r = \sqrt{2E}|\langle\Psi_k^{(r,-)}|\psi(\tau)\rangle|^2 \tag{16a}$$

$$\left(\frac{dP}{dE}\right)_l = \sqrt{2E}|\langle\Psi_k^{(l,-)}|\psi(\tau)\rangle|^2. \tag{16b}$$

For symmetric potentials $V(z)$, such as those considered here, Eqs. (16a) and (16b) can be related through time-reversal symmetry: $\Psi_k^{(r,+)}(z) = \Psi_k^{(l,-)*}(-z)$ and $\Psi_k^{(l,+)}(z) = \Psi_k^{(r,-)*}(-z)$, where $-z$ is the position coordinate reflection upon the potential center. It follows from Eqs. (10a) and (10b) that the total spectrum is simply the sum of the right and left contributions: $(dP/dE) = (dP/dE)_r + (dP/dE)_l$.

Figure 4 shows the spectra corresponding to rightward, leftward, and total emission for the same square well and laser pulse considered previously. First, we numerically verify that projecting onto the basis $\Psi_k^{(r,+)}$ and $\Psi_k^{(l,-)}$ yields equivalent results for rightward emission, and analogously, that $\Psi_k^{(l,+)}$ and $\Psi_k^{(r,-)}$ are equivalent for leftward emission. More importantly, we observe that while the left and right emission spectra are similar, they are not identical. As demonstrated in Ref. [29], strictly symmetric emission arises under symmetric pulses $F(t) = F(\tau - t)$ within the strong-field approximation (SFA). In our case, the pulse is symmetric and the potential is short-ranged, so the SFA provides an accurate description. The small deviations from perfect symmetry observed in Fig. 4 stem from the depletion of the ground state and the residual effect of the short-range potential on the escaping electron.[1] In this example, the total emission to the right (left) accounts for 49.88% (50.12%) of the total.

Now, we consider photoionization due to a short laser pulse with just two optical cycles, i.e., $\tau = 2 \times 2\pi/\omega = 15.71$ a.u.. In Fig. 5a, we plot the total energy spectrum calculated by projecting onto stationary eigenfunctions of the box, resulting in a highly oscillating distribution. By applying the WOM with $n = 3$ and $\gamma = 0.045$, we can smear the spurious oscillations rather efficiently; however, we still observe a reminiscence of these oscillations at high energy ($E \gtrsim 1.3$ a.u.). In addition, in the low energy part of the spectrum near threshold ($E \lesssim 0.05$ a.u.), the WOM spectrum falls off abruptly. This is an artifact of the method since it averages an energy region of width close to 2γ, whose one part lies in the continuum with appreciable transition probabilities ($E > 0$) and the other lies below the threshold ($E < 0$) with no eigenenergies close to it. Thus, the WOM average in Eq. (12) decreases as the energy approaches the threshold. Unlike the WOM, SPM succeeds in losing completely any reminiscence of the spurious oscillations in the energy spectrum and does not show any nonphysical fall-off behavior near threshold. For such a short pulse, the multiphoton peaks are absent in the photoelectron spectrum because of the broad band frequency components. Generally, as the laser pulse has a finite duration τ, the uncertainty relation $\Delta E \Delta t \sim 1$ leads

[1] The SFA is exact only for zero-range potentials and in the absence of initial state depletion.

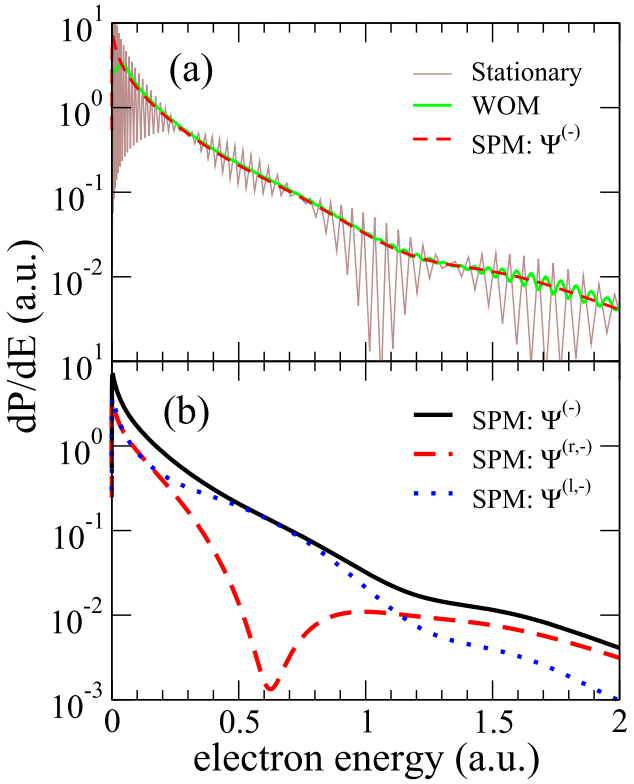

Fig. 5 Photoelectron spectrum from the only bound state of the same square well as in Figs. 2, 3, and 4, subject to one laser pulse with the same characteristics as in Figs. 2, 3, and 4 but with only two optical cycles of duration, i.e., $\tau = 15.71$ a.u.. **a** Projection of the spectrum onto stationary states with definite parity in thin brown solid line (highly oscillating), the spectrum projected onto the outgoing $\Psi^{(-)}$ in red dashed line and comparison to the spectrum calculated through the WOM with window width $\gamma = 0.045$ and $n = 3$ in green solid line. **b** Directional photoelectron spectrum calculated projecting the final wave function onto $\Psi^{(r,-)}$ and $\Psi^{(l,-)}$ together with their sum (projection onto $\Psi^{(-)}$) in dash red, dot blue, and solid black lines, respectively. The ionization toward the right (left) is 42.5% (57.5%)

to multiphoton peaks with a certain width $\Delta E \sim 1/\tau$. In this case, as the laser pulse comprises only two cycles, τ is small and the multiphoton peaks are very broad so that they overlap, which prevents their visualization. In Fig. 5b, the electron emission to the right $(dP/dE)_r$ and to the left $(dP/dE)_l$ are displayed. For this such short laser pulse, we observe a rather asymmetric distribution, except near threshold. In particular, the total emission to the right (left) is 42.5% (57.5%) of the total ionization probability $P_{\rm ion} = 0.64$ in this case. As expected, the right-left asymmetry is enhanced when the pulse duration is shortened (compare Figs. 4 and 5).

In order to produce very asymmetric electron emission, we consider half-cycle pulses of the form

$$F(t) = -F_0 \sin^2\left(\frac{\pi t}{\tau}\right), \tag{17}$$

for $0 < t < \tau$ and zero elsewhere. These short electric fields of duration in the order of the picoseconds do not represent traveling waves and have been developed for the production of quasi-one-dimensional very-high-n Rydberg atoms [30] and inducing focusing of Rydberg wave packets in the phase space [31]. However, in this work we will use pulses much shorter than the excursion time of the initial state, i.e., $\tau \ll 2a/\sqrt{2I_p}$ (in the order of the attoseconds) to ensure that we are in the sudden regime where the electric field of Eq. (17) can be thought of as a single kick of momentum transfer $\Delta p = -\int_0^\infty dt F(t)$ when they interact with the electron initially bound to the square-well potential used [32,33]. In Fig. 6, we show the directional (right and left) emission spectrum from the same square well of Figs. 2, 3, 4, and 5 subject to the half-cycle pulse [Eq. (17)] of duration $\tau = 1$ a.u. and momentum transfers $\Delta p = 0.05$ a.u. and $\Delta p = 0.5$ a.u. in Fig. 6a and b, respectively. We observe that there is more emission toward the right than toward the left for both kick strengths, which is anticipated from a classical viewpoint, since negative kicks push the electron (of negative charge) toward the right. As expected, when the kick strength is increased, the right-left emission asymmetry increases. For $\Delta p = 0.05$, the emission to the right (left) is 57% (43%) of the total ionization probability is $P_{\rm ion} = 3 \times 10^{-4}$, whereas for $\Delta p = 0.5$, the emission to the right (left) is 92% (8%) of the total ionization $P_{\rm ion} = 0.27$.

For a closer inspection of the emission asymmetry for half-cycle pulses, we define the total asymmetry factor as

$$A = \frac{(P_{\rm ion})_r - (P_{\rm ion})_l}{P_{\rm ion}}, \tag{18}$$

where $(P_{\rm ion})_r = \int_0^\infty dE\,(dP/dE)_r$, $(P_{\rm ion})_l = \int_0^\infty dE\,(dP/dE)_l$, and $P_{\rm ion} = (P_{\rm ion})_r + (P_{\rm ion})_l$, and the differential asymmetry factor as

$$A(E) = \frac{\left(\frac{dP}{dE}\right)_r - \left(\frac{dP}{dE}\right)_l}{\left(\frac{dP}{dE}\right)}. \tag{19}$$

The asymmetry factors [Eq. (18)] for the right-left spectra of Fig. 5b, Fig. 6a, and Fig. 6b are $A = -0.15, 0.15$, and 0.84, respectively. In Fig. 7, we show the asymmetry factor A defined in Eq. (18) as a function of the magnitude of the momentum transfer Δp for ionization by a half-cycle pulse of duration $\tau = 1$ a.u.. We clearly observe that the asymmetry factor increases monotonically as the momentum transfer increases in magnitude, tending to unity, which means that all the ionization will be toward the right and, on the other hand, for weak momentum transfers the asymmetry approaches to zero, as expected [31]. In the inset, we show the differential asymmetry coefficient $A(E)$ defined in Eq. (19) and observe that different momentum transfers impacts differently on the emission asymmetry depending on the kinetic energy of the escaping electron.

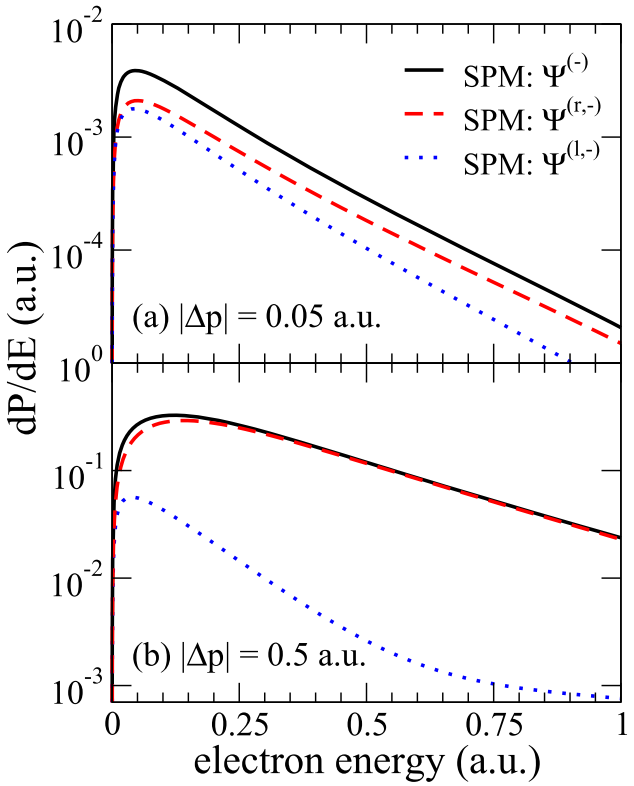

Fig. 6 Photoelectron spectrum from the only bound state of the same square well in Figs. 2, 3, 4, and 5 subject to a half-cycle pulse of duration $\tau = 1$ a.u. and momentum transfer $\Delta p = 0.05$ a.u. in (**a**) and $\Delta p = 0.5$ a.u. in (**b**). The spectrum projected onto the respective incoming scattering waves from right and the left $\Psi^{(r,-)}$ and $\Psi^{(l,-)}$ together with their sum (projection onto $\Psi^{(-)}$) in dash red, dot blue, and solid black lines, respectively

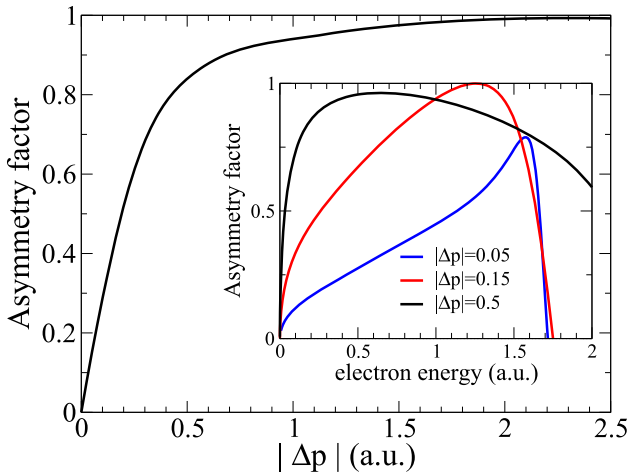

Fig. 7 Asymmetry factor A as a function of the magnitude of the momentum transfer $|\Delta p|$ for ionization by a half-cycle pulse of duration $\tau = 1$ a.u.. Inset: differential asymmetry factor $A(E)$ as a function of the energy for three different momentum transfers: $\Delta p = 0.05$, 0.15, and 0.5 in blue, red, and black lines, respectively

4 Applications to metallic surfaces

In this section, we apply our study on the retrieval of the energy spectrum and the elimination of spurious oscillations to photoemission from metallic surfaces. We consider grazing incidence of an ultrashort laser pulse of duration in the range from femto- to attoseconds on a metallic surface. We characterize the pulse as a time-dependent electric field linearly polarized along $\hat{\mathbf{z}}$, perpendicular to the solid surface within the dipole approximation. Because of this interaction, the solid is ionized, so that an electron located in the valence band of the solid is promoted to the continuum. Using the single active electron (SAE) approximation, the total Hamiltonian is described as

$$H(\mathbf{r}, t) = -\frac{\nabla_r^2}{2} + V_S(z) + zF(t), \tag{20}$$

where $-\nabla_r^2/2$ is the electron kinetic energy, $V_S(z)$ is the potential that represents the electron–surface interaction and $zF(t)$ accounts for the interaction of the active electron with the electric field, within the length gauge. We consider a laser pulse of the form of Eq. (14). The Hamiltonian in Eq. (20) can be separated in the Cartesian coordinates $H(x, y, z, t) = H_x(x) + H_y(y) + H_z(z, t)$ with $H_x(x) = -\partial^2/\partial x^2$ and $H_y(y) = -\partial^2/\partial y^2$ corresponding to the Hamiltonian of a free particle, and

$$H_z(z, t) = -\partial^2/\partial z^2 + V_S(z) + zF(t), \tag{21}$$

corresponding to a one-dimensional model of the surface. The electron dynamics is determined by the TDSE in Eq. (1). As the solutions of $H_x(x, t)$ and $H_y(y, t)$ are just plane waves, we circumscribe our problem to solve the TDSE in the $\hat{\mathbf{z}}$ direction perpendicular to the solid surface.

4.1 Jellium surface model

First, we analyze photoemission for the simplest possible model for the electron–surface interaction: the jellium model, where the electron–surface interaction is modeled as a slab of width a and depth $V_0 = E_F + \Phi$, corresponding to a Fermi energy E_F and a work function of the metal surface Φ, thus

$$V_S(z) = -V_0\Theta(a/2 - |z|). \tag{22}$$

As the room temperature is much less than the Fermi temperature of metals, the initial state corresponds to a set of electrons with energy levels below the Fermi level (from the bottom of the potential well), i.e., $-V_0 < E < -V_0 - E_F = -\Phi$, due to the Pauli exclusion principle (see Fig. 8). Therefore, we must calculate the photoelectron spectrum as [34]

$$\frac{dP}{dE} = 2\sqrt{2E}\rho(E)\sum_i |a_{ik}|^2\Theta(-E_i - \Phi), \tag{23}$$

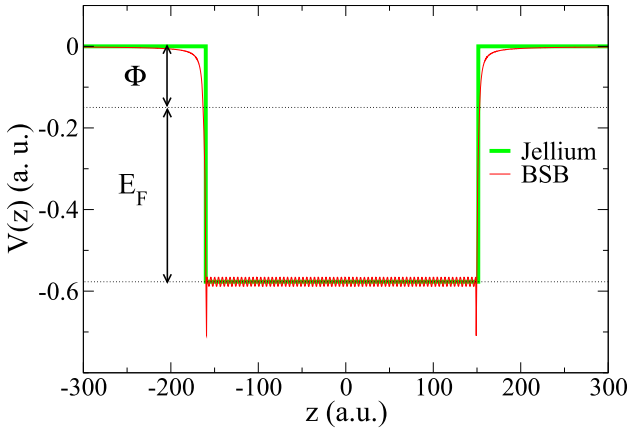

Fig. 8 Jellium (thick green line) and BSB (thin red line) model potentials for the metallic surface Al(111) with $E_F = 0.414$ a.u., $\Phi = 0.156$ a.u., and $a = 311.54$ a.u

where the factor 2 arises from spin independence and $\rho(E)$ is the density of final continuum states with final electron momentum perpendicular to the surface $k = \sqrt{2E}$. The Heaviside function $\Theta(-E_i - \Phi)$ restricts the initial states to those contained within the Fermi sphere (reduced to an energy segment in our 1D treatment), where E_i is the initial bound electron energy.

We solve the one-dimensional TDSE corresponding to the problem of photoemission perpendicular to Al(111) surface for the jellium model Eq. (22) using $a = 400$ a.u., and $V_0 = E_F + \Phi = 0.57$ corresponding to a Fermi energy $E_F = 0.414$ a.u. and a work function of the metal surface $\Phi = 0.156$ a.u.. We consider the ionization of Al(111) due to grazing incidence of a laser pulse of electric field amplitude $F_0 = 0.1$ a.u., frequency $\omega = 1$ a.u. and duration equal to $\tau = 40$ a.u.. By solving the TDSE via a finite difference method, we get the corresponding time-evolved wave function at the end of the laser pulse $\psi(z, \tau)$. Then, we project $\psi(z, \tau)$ onto the stationary continuous eigenfunctions of the time-independent part of the Hamiltonian in Eq. (21) and get the transition coefficients whose modulus squared represents the emission probability of the electron into the vacuum region with energy $E = k^2/2$ [see Eq. (6)]. In this case, we solve the TDSE in Eq. (1) with the Hamiltonian of Eq. (21) discretizing the position with a numerical mesh of width $L = 800$ a.u. and spacing $\Delta z = 0.1$ a.u.. We compute the time propagation up to the end of the laser pulse τ using a time step $\Delta t = 4.05 \times 10^{-4}$ a.u.. The aforementioned unperturbed Hamiltonian of Eq. (21) with the jellium potential in Eq. (22) is diagonalized [28], resulting in 136 bound eigenstates, from which 116 are initially occupied below the Fermi level, and 507 continuum eigenstates. Because the jellium potential is even with respect to the center of the well, eigenstates of the time-independent part of H_z in Eq. (21) are even or odd [24]. In addition, the corresponding time-evolved wave function for the typical laser intensities considered is only subtly nonsymmetrical. We then project

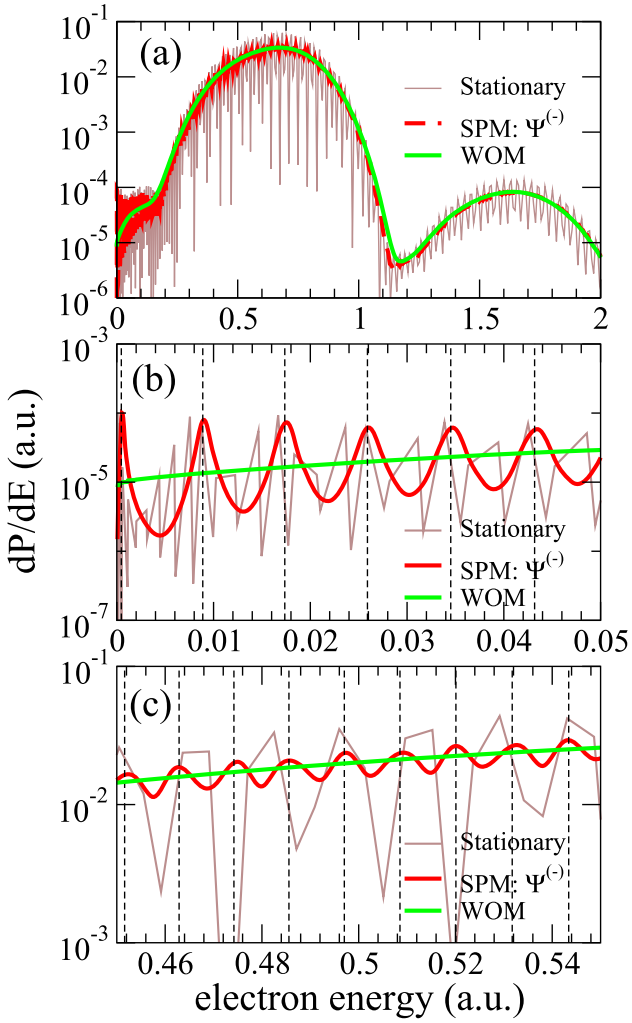

Fig. 9 **a** Photoelectron spectrum perpendicular to the surface Al(111) within the jellium model: $\Phi = 0.156$ a.u., $E_F = 0.414$ a.u., $a = 400$ a.u., $V_0 = 0.57$ a.u.. Projection onto stationary states of definite parity in brown thin solid line (highly oscillating) and projection onto outgoing states $\Psi^{(-)}$ in red dashed solid line and the WOM spectrum in thick solid green line ($\gamma = 0.045$ a.u. and $n = 3$). Close up for the ranges **b** $0 < E < 0.05$ near threshold and (c) $0.45 < E < 0.55$ near the top of the first multiphoton peak. Vertical dash lines correspond to Ramsauer–Townsend resonances, i.e., $E_j = j^2\pi^2/(2a^2) - V_0$ with $V_0 = \Phi + E_F$. Laser pulse parameters are $F_0 = 0.1$ a.u., $\omega = 1$ a.u., and $\tau = 40$ a.u.

the time-evolved wave function at the end of the pulse, $\psi(z, \tau)$, onto the stationary eigenstates of the numerical box with eigenenergies $E > 0$ (representing the continuum), which results in the energy spectrum with huge oscillations spanning about two orders of magnitude shown with a thin red line of Fig. 9 as reported in previous works [12,14,26]. The corresponding projections on the stationary eigenstates result in high or low values depending on whether the parity of the time-evolved wave function matches or not the parity of the continuum eigenstate, respectively. Consequently, we obtain

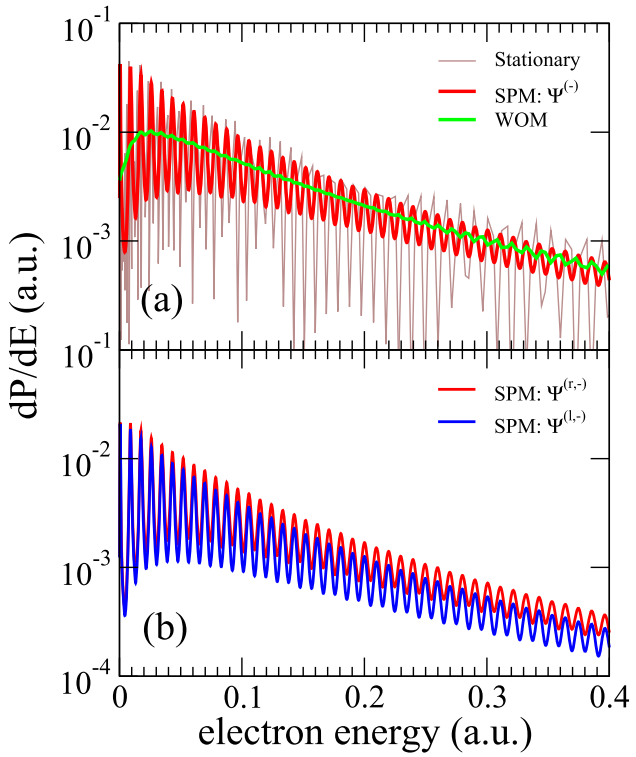

Fig. 10 Photoelectron spectrum perpendicular to the surface for Al(111) within the jellium model: $\Phi = 0.156$ a.u., $E_F = 0.414$ a.u., $a = 400$ a.u., $V_0 = 0.57$ a.u. subject to a half-cycle pulse of duration $\tau = 1$ a.u. and momentum transfer $\Delta p = -0.05$ a.u.. **a** Projection onto eigenfunctions of the TISE with definite parity in brown thin solid line (highly oscillating), projection onto outgoing states $\Psi^{(-)}$ in red solid line and WOM spectrum in thick green line ($\gamma = 0.01$ a.u. and $n = 3$). **b** Directional spectra calculated by projecting the final wave function onto $\Psi^{(r,+)}$ and $\Psi^{(l,+)}$ in red and blue lines, respectively

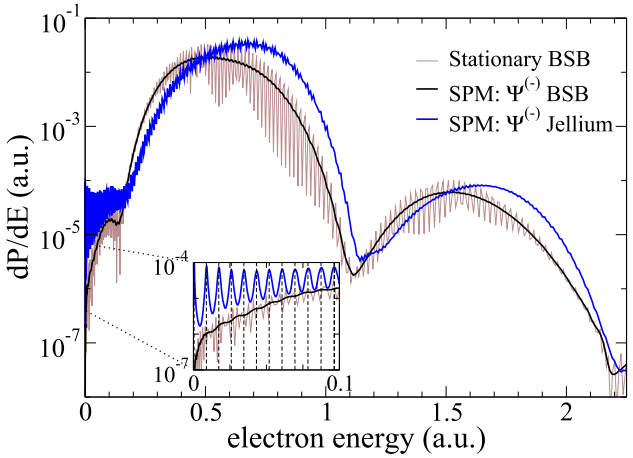

Fig. 11 Photoelectron spectrum perpendicular to the surface Al(111) within the BSB model: $\Phi = 0.156$ a.u., $E_F = 0.414$ a.u., and $a = 311$ a.u. subject to the same laser pulse of Fig. 9. Projection onto stationary states with definite parity in brown line (highly oscillating) and onto outgoing scattering waves $\Psi^{(-)}$ in black line. We compare the results with the projection onto scattering waves of the spectrum corresponding to the jellium model in blue line. The inset shows that the Ramsauer–Townsend resonances present in the jellium model almost vanish in the BSB model

the very oscillating spectrum in Fig. 9a. We observe the multiphoton peaks at $E \simeq 0.7$ a.u. and 1.7 a.u. separated by the photon energy $\omega = 1$ a.u.. We use the WOM with width parameter $\gamma = 0.045$ a.u. and $n = 3$ to smooth the spectrum, which is observed in green solid line in the whole energy range. SPM results also in a smooth spectrum in the high-energy region but many oscillations arises for $E \lesssim 0.8$ a.u. The amplitude of these high-frequency oscillations increases substantially as the energies approach the threshold. We show a close-up of Fig. 9a near threshold in Fig. 9b and near the first multiphoton peak in Fig. 9c. We observe that the high oscillations exposed by the SPM have a spacing which increases with the electron kinetic energy and perfectly matches the eigenenergies of the infinite well of width a and depth V_0, indicated with vertical dashed lines. This is a proof that these high-frequency oscillations are of the different nature from the spurious high-frequency oscillations when projecting on stationary eigenstates of the box with definite parity. The oscillations captured by the SPM corresponds to Ramsauer–Townsend oscillations coming from the interference of the traveling waves bouncing against the sharp edges of the well with energies $E_j = j^2\pi^2(2a^2) - V_0$. We clearly see that the SPM accounts accurately for any high-frequency physically meaningful oscillation in the energy spectrum whereas the WOM overlooks such resonances. However, if the potential well described a finite system such as nanostructures or quantum dots, Ramsauer–Townsend oscillations or any kind of high-frequency oscillation do have a physical meaning and would be completely overlooked by the WOM. However, for the particular case of photoionization from a metallic surface, in the limit of $a \to \infty$ Ramsauer–Townsend oscillations must disappear.

When a half-cycle pulse of duration $\tau = 1$ and momentum transfer $\Delta p = 0.05$ a.u. is applied to the Al(111) surface modeled with the jellium model, we observe in Fig. 10a that the highly oscillating total spectrum calculated by projecting onto the stationary states of the continuum is completely smoothed by the WOM using a window width $\gamma = 0.0045$ a.u. and $n = 3$. However, the SPM accounts for the Ramsauer–Townsend oscillations with high precision. In Fig. 10b, we show emission in both directions calculated within the SPM, also displaying Ramsauer–Townsend resonances. The emission to the right (left) is the 57% (43%) of a very low ionization probability $P_{\text{ion}} = 2 \times 10^{-5}$.

4.2 Band-structure-based surface model

Finally, we solve the problem of photoionization of a metal surface in which case the potential $V_S(z)$ in Eq. (20) is replaced by the more realistic band-structure-based (BSB) potential where the surface is represented

as a collection of atomic planes that together form a *slab* and takes into account effects of the band structure of the metal [20]. The BSB potential is illustrated in Fig. 8 for the case of Al(111). We solve Eq. (1) using the BSB potential for an Al(111) surface and calculate the perpendicular photoemission probability produced by the same laser pulse of Fig. 9. A grid of length $L = 789.84$ a.u. spacing $\Delta z = 0.05$ a.u. with time step $\Delta t = 0.000405$ a.u. is used. After diagonalization [28] of the BSB potential, we obtain 120 bound eigenstates, from which 91 are occupied below the Fermi level ($E < E_F$), and 467 continuum eigenstates. In Fig. 11, we compare the total emission calculated with the projection onto stationary eigenstates using Eq. (6) and the SPM. Unlike square-well potentials, in the case of the BSB potential the scattering waves do not have any analytical solution and are unknown [25]. In consequence, in order to implement the SPM we must appeal to the procedure described in the Appendix A (from step 1 to step 7) to obtain the numerically converged outgoing scattering basis $\{\Psi_k^{(-)}(z)\}$ computed using a minimization tolerance of 10^{-12}. Again, spurious oscillations are correctly eliminated within the SPM. When comparing the total energy spectrum calculated within the two models: BSB and jellium, two important things are worth mentioning. First, there is a shift of about 0.15 a.u. in the position of the peaks, which is the BSB spectrum displaced toward the threshold with respect to the jellium spectrum. This shift was adjudicated to the rugosity of the BSB potential [12,13,34]. Very importantly, the Ramsauer–Towsend oscillations in the jellium spectrum are washed out in the BSB model because the surface potential is described with smooth walls.

5 Conclusions

We have introduced the scattering projection method (SPM) to retrieve the energy spectrum in one-dimensional photoionization problems. SPM is based on solving the time-dependent Schrödinger equation, and projected the final time-evolved wave function onto scattering waves that have appropriate incoming or outgoing boundary conditions. This approach was developed to eliminate spurious oscillations that often appear in the ionization spectrum when using a numerical basis generated on a finite grid. We compared our method to another commonly used technique for reducing spurious oscillations, the well-known window-operator method (WOM), and demonstrated several advantages of SPM. On the one hand, SPM smooths more effectively high-frequency oscillations compared to WOM. Additionally, SPM enables the computation of directional emission, allowing for the investigation of emission asymmetry. We have also studied this asymmetry using directional half-cycle pulses.

In practical applications, such as the electron emission from metal surfaces excited by the grazing incidence of ultrashort laser pulses, previous calculations faced significant challenges from numerous spurious oscillations. Our new results show that SPM can resolve certain physical features in the spectra from metal surfaces while disregarding spurious oscillations. Overall, SPM produces smoother ionization spectra more efficiently than WOM, and, importantly, it does not remove other types of physical oscillations that mainly arise from genuine quantum interference effects.

Acknowledgements This work is supported by PICT Grants No. 2020–01755, No. 2020–01434, and No. 2020–01931 of ANPCyT (Argentina), PIP Grant No. 2022–2024 No 11220210100468CO and No. 11220200102421CO of Consejo Nacional de Investigaciones Científicas y Técnicas (CONICET) (Argentina).

Author contributions

All authors contributed equally to this work.

Data Availability Statement Data will be made available on reasonable request [Authors' comment: The datasets generated during and/or analysed during the current study are available from the corresponding author on reasonable request [mbarlari@iafe.uba.ar].

Appendix A. Numerical calculation of the scattering waves

We assume a localized one-dimensional potential ($V(z) \neq 0$ for $z_0 < z < z_1$) and an incident particle from the left. Since in all our cases the potential is asymptotically zero in the external region, the wave function $\Psi_k^{(l,-)}(z)$ in Eq. (8b) can be divided in three different regions:

$$\Psi_k^{(l,-)}(z) = \begin{cases} \phi_I(z) & \text{if } z < z_0 \\ \phi_{II}(z) & \text{if } z_0 < z < z_1 \\ \phi_{III}(z) & \text{if } z > z_1. \end{cases} \tag{A.1}$$

First, the transmission $\left|T_l^{(-)}\right|^2$ and reflection $\left|R_l^{(-)}\right|^2$ coefficients must satisfy $\left|T_l^{(-)}\right|^2 + \left|R_l^{(-)}\right|^2 = 1$. Then, the boundary conditions at the edges z_0 and z_1 are established, requiring the continuity of the wave function and its derivative. The proposed procedure to obtain $\Psi_k^{(l,-)}(z)$ is the following [25]:

(i) Given the energy of the incident particle E, an initial value of the complex reflection parameter $R_l^{(-)}$ is proposed, which must be restricted to a unit circle because $\left|R_l^{(+)}\right|^2 \leq 1$.

(ii) Applying the continuity criteria, in Eq. (A.1) we use the function $\phi_I(z)$ to determine the function $\phi_{II}(z)$ and its derivative at the point z_0.
(iii) The time-independent Schrödinger equation is solved in the intermediate region by integrating from z_0 to z_1 using the fourth-order Runge–Kutta method [22].
(iv) Knowing the function $\phi_{II}(z_1)$, and applying the continuity conditions to Eq. (A.1), the right-hand side function $\phi_{III}(z)$ is obtained. With it, we get the transmission coefficient given by $T_l^{(-)}(k) = \phi_{III}(z_1)\, e^{ikz_1}$.
(v) Using this value of the transmission coefficient $T_l^{(+)}(k)$, the equation is integrated in the opposite direction (from z_1 to z_0), obtaining, in the central region of Eq. (A.1), a new $\phi_{II}(z)$.
(vi) On the left edge z_0, the continuity conditions are applied, determining $\phi_I(z_0)$. This allows obtaining a new complex reflection coefficient $R_l^{(-)}\Big|_{\text{new}} = \left[\phi_{II}(z_0) - e^{ikz_0}\right] e^{ikz_0}$ from Eq. (9b). We define a real function that corresponds to the Euclidean distance between the old and new reflection coefficients $R_l^{(-)}$ and $R_l^{(-)}\Big|_{\text{new}}$.
(vii) An iteration process is performed, such that it minimizes the distance between the old and new reflection coefficients $R_l^{(-)}$ and $R_l^{(-)}\Big|_{\text{new}}$. The integration problem is now transformed into an optimization problem. In the present work, this is done using the *steepest descent* method [22].

In a completely analogous way, we solved the problem of an incident particle from the right, in which case the scattering wave function $\Psi_k^{(r,-)}(z)$ is obtained. The combination of both types of functions, calculated at different energies, constitutes a complete scattering basis. We proceed analogously with $\Psi_k^{(l,+)}$ and $\Psi_k^{(r,+)}$.

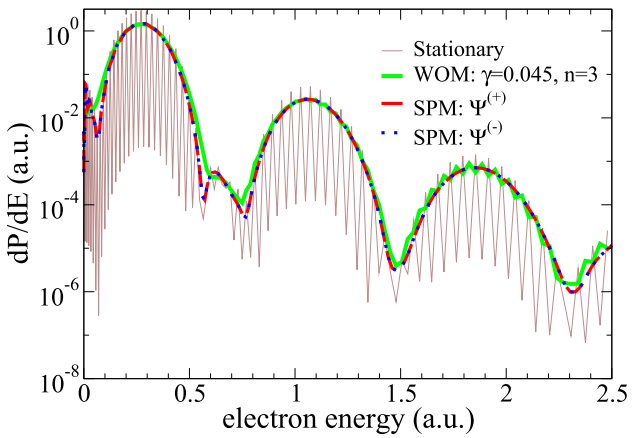

Fig. 12 Photoelectron emission probabilities for the soft-core potential of Eq. B.1 from ϕ_1. Thin brown solid line: projection onto L^2 stationary eigenstates. Solid red line: $(dP/dE)^{(+)}_{\text{SPM}}$, i.e., projection onto incoming $\Psi^{(+)}$ scattering wave. Dash blue line: $(dP/dE)^{(-)}_{\text{SPM}}$. Green line: window filtered spectra with $\gamma = 0.045$ and $n = 3$

Appendix B. Soft-core hydrogenic potential

We calculate the photoelectron spectrum for a soft-core model potential of the form

$$V(z) = -\frac{V_0}{\sqrt{\alpha + z^2}}\,, \tag{B.1}$$

using $V_0 = 0.779532$ and $\alpha = 1$, the potential yields a ground-state energy of $E = -0.5$ a.u., corresponding to that of a hydrogen atom [35–38]. In Fig. 12, we show the photoelectron spectrum from the ground state, calculated using both the WOM and the SPM. We observe that the same conclusions discussed in the main text for the square-well potential also hold for the soft-core potential.

References

1. P. Dombi, M. Schultze, The Nobel prize in physics 2023. Europhys. News **54**(5), 8–9 (2023)
2. P. Agostini, F. Fabre, G. Mainfray, G. Petite, N.K. Rahman, Free-free transitions following six-photon ionization of xenon atoms. Phys. Rev. Lett. **42**, 1127–1130 (1979)
3. L.F. Dimauro, P. Agostini, Ionization dynamics in strong laser fields. Adv. At. Mol. Opt. Phy. **35**, 79–120 (1995)
4. M. Schultze, M. Fieß, N. Karpowicz, J. Gagnon, M. Korbman, M. Hofstetter, S. Neppl, A.L. Cavalieri, Y. Komninos, T. Mercouris, C.A. Nicolaides, R. Pazourek, S. Nagele, J. Feist, J. Burgdörfer, A.M. Azzeer, R. Ernstorfer, R. Kienberger, U. Kleineberg, E. Goulielmakis, F. Krausz, V.S. Yakovlev, Delay in photoemission. Science **328**(5986), 1658 (2010)
5. F. Krausz, M. Ivanov, Attosecond physics. Rev. Mod. Phys. **81**, 163–234 (2009)
6. A.D. Dutoi, M. Wormit, L.S. Cederbaum, Ultrafast charge separation driven by differential particle and hole mobilities. J. Chem. Phys. **134**(2), 024303–024303 (2011)
7. M. Huppert, I. Jordan, D. Baykusheva, A. von Conta, H.J. Wörner, Attosecond delays in molecular photoionization. Phys. Rev. Lett. **117**(9), 093001 (2016)
8. Q.-C. Ning, L.-Y. Peng, S.-N. Song, W.-C. Jiang, S. Nagele, R. Pazourek, J. Burgdörfer, Q. Gong, Attosecond streaking of Cohen-Fano interferences in the photoionization of H2+. Phys. Rev. A **90**(1), 013423 (2014)
9. A.L. Cavalieri, N. Müller, T. Uphues, V.S. Yakovlev, A. Baltuška, B. Horvath, B. Schmidt, L. Blümel, R. Holzwarth, S. Hendel, M. Drescher, U. Kleineberg, P.M. Echenique, R. Kienberger, F. Krausz, U. Heinzmann, Attosecond spectroscopy in condensed matter. Nature **449**(7165), 1029–1032 (2007)
10. S. Neppl, R. Ernstorfer, E.M. Bothschafter, A.L. Cavalieri, D. Menzel, J.V. Barth, F. Krausz, R. Kien-

berger, P. Feulner, Attosecond time-resolved photoemission from core and valence states of magnesium. Phys. Rev. Lett. **109**, 087401 (2012)
11. M. Ossiander, J. Riemensberger, S. Neppl, M. Mittermair, M. Schäffer, A. Duensing, M.S. Wagner, R. Heider, M. Wurzer, M. Gerl, M. Schnitzenbaumer, J.V. Barth, F. Libisch, C. Lemell, J. Burgdörfer, P. Feulner, R. Kienberger, Absolute timing of the photoelectric effect. Nature **561**(7723), 374–377 (2018)
12. C.A.R. Rubiano, M.S. Gravielle, D.M. Mitnik, V.M. Silkin, Band-structure effects in photoelectron-emission spectra from metal surfaces. Phys. Rev. A **85**(4), 043422 (2012)
13. C.A.R. Rubiano, R.D. Picca, D.M. Mitnik, V.M. Silkin, M.S. Gravielle, Induced-field enhancement of band-structure effects in photoelectron spectra from Al surfaces by ultrashort laser pulses. Phys. Rev. A **95**(3), 033401 (2017)
14. M.N. Faraggi, M.S. Gravielle, D.M. Mitnik, Interaction of ultrashort laser pulses with metal surfaces: Impulsive jellium-Volkov approximation versus the solution of the time-dependent Schrödinger equation. Phys. Rev. A **76**(1), 012903 (2007)
15. B. Fetić, W. Becker, D.B. Milošević, Extracting photoelectron spectra from the time-dependent wave function: Comparison of the projection onto continuum states and window-operator methods. Phys. Rev. A **102**(2), 023101 (2020)
16. B. Fetić, M. Tunja, W. Becker, D.B. Milošević, Extracting photoelectron spectra from the time-dependent wave function. II. Validation of two methods: Projection on plane waves and time-dependent surface flux. Phys. Rev. A **105**(5), 053121 (2022)
17. K. Amini, A. Chacón, S. Eckart, B. Fetić, M. Kübel, Quantum interference and imaging using intense laser fields. European Phys. J. D **75**(10), 275 (2021)
18. K.J. Schafer, K.C. Kulander, Energy analysis of time-dependent wave functions: Application to above-threshold ionization. Phys. Rev. A **42**(9), 5794–5797 (1990)
19. K.J. Schafer, The energy analysis of time-dependent numerical wave functions. Comput. Phys. Commun. **63**(1–3), 427–434 (1991)
20. E.V. Chulkov, V.M. Silkin, P.M. Echenique, Image potential states on metal surfaces: binding energies and wave functions. Surf. Sci. **437**(3), 330–352 (1999)
21. C. Moler, C. van Loan, Nineteen Dubious Ways to Compute the Exponential of a Matrix. Twenty-Five Years Later. SIAM Review **45**(1), 3–49 (2003)
22. W.H. Press, S.A. Teukolsky, W.T. Vetterling, B.P. Flannery. *Numerical Recipes 3rd Edition: The Art of Scientific Computing*. Cambridge University Press, 3 edition, (2007)
23. M.S. Pindzola, F. Robicheaux, S.D. Loch, J.C. Berengut, T. Topcu, J. Colgan, M. Foster, D.C. Griffin, C.P. Ballance, D.R. Schultz, T. Minami, N.R. Badnell, M.C. Witthoeft, D.R. Plante, D.M. Mitnik, J.A. Ludlow, U. Kleiman, TOPICAL REVIEW: The time-dependent close-coupling method for atomic and molecular collision processes. J. Phys. B Atomic Mol. Phys. **40**(7), R39–R60 (2007)
24. D.J. Griffiths, D.F. Schroeter, *Introduction to quantum mechanics* (Cambridge University Press, Cambridge; New York, NY, third edition edition, 2018)
25. T. Pang, *An introduction to computational physics*, 2nd edn. (Cambridge University Press, Cambridge, 2006)
26. A.E. Garriz, A. Sztrajman, D. Mitnik, Running into trouble with the time-dependent propagation of a wavepacket. Eur. J. Phys. **31**(4), 785–799 (2010)
27. D. Bauer, P. Koval, QPROP: A Schrödinger-solver for intense laser atom interaction. Comput. Phys. Commun. **174**(5), 396–421 (2006)
28. National Science Foundation and Department of Energy. LAPACK – linear algebra PACKage. http://www.netlib.org/lapack/, (2010)
29. D.G. Arbó, J.E. Miraglia, M.S. Gravielle, K. Schiessl, E. Persson, J. Burgdörfer, Coulomb–Volkov approximation for near-threshold ionization by short laser pulses. Phys. Rev. A **77**(1), 013401 (2008)
30. C.L. Stokely, J.C. Lancaster, F.B. Dunning, D.G. Arbó, C.O. Reinhold, J. Burgdörfer, Production of quasi-one-dimensional very-high-n Rydberg atoms. Phys. Rev. A **67**(1), 013403 (2003)
31. D.G. Arbó, C.O. Reinhold, J. Burgdörfer, A.K. Pattanayak, C.L. Stokely, W. Zhao, J.C. Lancaster, F.B. Dunning, Pulse-induced focusing of Rydberg wave packets. Phys. Rev. A **67**(6), 063401 (2003)
32. D.G. Arbó, K. Tőkési, J.E. Miraglia, Limitations of the strong field approximation in ionization of the hydrogen atom by ultrashort pulses. Eur. Phys. J. D **51**(3), 303–312 (2009)
33. D.G. Arbó, M.S. Gravielle, K.I. Dimitriou, K. Tőkési, S. Borbély, J.E. Miraglia, Ionization of the hydrogen atom by short half-cycle pulses: dependence on the pulse duration. Eur. Phys. J. D **59**(2), 193–200 (2010)
34. C.A.R. Rubiano. *Interacción dinámica rápida de partículas y campos electromagnéticos con superficies metálicas*. PhD thesis, Universidad de Buenos Aires - CONICET. Instituto de Astronomía y Física del Espacio (IAFE). Grupo de Dinámica Cuántica en la Materia, https://bibliotecadigital.exactas.uba.ar/collection/tesis/document/tesis_n5685_RiosRubiano, (2015)
35. X. Zhou, C.D. Lin, Linear-least-squares fitting method for the solution of the time-dependent Schrödinger equation: Applications to atoms in intense laser fields. Phys. Rev. A **61**(5), 053411 (2000)
36. J. Wassaf, V. Véniard, R. Taïeb, A. Maquet, Strong Field Atomic Ionization: Origin of High-Energy Structures in Photoelectron Spectra. Phys. Rev. Lett. **90**(1), 013003 (2003)
37. Q. Su, J.H. Eberly, Model atom for multiphoton physics. Phys. Rev. A **44**(9), 5997–6008 (1991)
38. R. Dehnen, V. Engel, Wave-packet dynamics and photoionization in the Coulomb potential. Phys. Rev. A **52**(3), 2288–2294 (1995)